A Detailed Solution Framework for the Out-of-Plane Displacement of Circular Dielectric Elastomer Actuators

Daniel Korn[1], Carson Farmer[2], and Hector Medina *[2]

[1] *Purdue University, 610 Purdue Mall, West Lafayette, IN, 47907*
[2] *Liberty University, 1971 University Blvd. Lynchburg, VA, 24515*

Abstract

The out-of-plane displacement (OPD) of a circular dielectric elastomer actuator (DEA) membrane has been explored in recent years for a variety of important applications. Circular DEAs consist of an elastomer membrane that is prestretched to a rigid frame and coated with compliant electrodes. Such a simple configuration has found many interesting applications such as in, pumps, pulse tracking, hopping search and rescue robots, dielectric elastomer (DE) generators for renewable energy harvesting, linear actuators, and many others. Here, we present an easy-to-follow implementation of the OPD equations for circular DEAs via a detailed numerical solution using the shooting method (SM) on a system of differential algebraic equations (DAE), based on previous theoretical work. The SM numerical solution to the system of DAEs is applied to a practical range of values based on the reported literature. Analysis of the results and comparison against other studies are provided. The current work provides a go-to framework for implementation in further research and development.

1 Introduction

A circular dielectric elastomer actuator (DEA) can consist of an elastomeric membrane that is prestretched over a rigid frame and is covered with a compliant electrode (see Fig. 1). Depending on the desired actuation, numerous configurations of electrodes can be used. The membrane is then displaced out of plane using a variety of means such as a spring, biasing mass, or magnet [1]. This "cone" is then utilized as a means of inhomogeneous actuation, sometimes in conjunction with other mechanisms. Actuators made in such way can be used for multiple applications, as they can exhibit motion with large ranges, high prescribability, smoothness, reasonable bandwidth of $\mathcal{O}(10^0)$ to $\mathcal{O}(10^3)$ Hz, and capability of resonance. Some applications of devices that rely on the out-of-plane motion of circular DEAs are surveyed in the sequel.

Cao et al. [2] proposed a novel pneumatic diaphragm pump where two circular membranes with a diameter of 30 mm are held apart via permanent magnets and deformed out of plane by applying a voltage across the compliant electrodes. Each elastomer is actuated in turn while the other acts passively causing air to be sucked into a chamber and forced out again through one-way valves. While only using 40 mW, this pump is capable of producing pressures up to 30.5 mbar and a rate of 0.9 SLPM (Standard Liter Per Minute) by capitalizing on the effects of resonance that greatly amplifies the stroke while minimizing power consumption. The lowest power consumption was achieved around 79 Hz. Linnebach et al. [3] proposed a different variation of a pneumatic diaphragm pump. Their pump consists of a 45 mm diameter circular DEA that is deformed out of plane using a spring. Unlike the design proposed by Cao et al. [2], Linnebach et al. only used one DEA in conjunction with a diaphragm that is controlled by actuating the DEA. This action moves the air through the system by utilizing check valves. They were able to achieve 192.25 mbar and a flowrate of 1.48 SLMP with a voltage of only 3 kV at an optimal frequency of 98.11 Hz.

Ye et al. [4] used a circular DEA deforming out of plane to validate the pulse-tracking ability of a conical DEA. A 69mm diameter circular elastomer was used that was deformed out of plane using a biasing mass. The device received an input signal based on an actual human pulse. This was converted to the corresponding displacement of the actuator. Using an H_∞ control, the device was able to track the pulse signal albeit with

*Corresponding author: hmedina@liberty.edu

better results for the low-frequency components of the signal. By using a load cell, another aspect was able to be tested. The actuator was also able to produce a pressure to mirrored that of the measured human pulse. Dubowsky et al. [5] investigated the use of a circular DEA deforming out of plane to power a hopping search and rescue robot. This 46 g robot was comprised of a 10.5 cm diameter spherical housing with a power source providing 8.8 kV and a single DEA that would be actuating 35 times to store energy in a spring via a ratcheting mechanism. Once enough energy was stored, the "microbot" would launch into the air achieving heights of up to 38 cm.

Bortot and Gei [6] explored the feasibility of using a circular DEA deforming out of plane as a dielectric elastomer generator to harvest renewable energy. This was accomplished through a four-phase cycle of mechanical loading, electrical charging, mechanical discharging, and electrical discharging. An efficiency higher than 26% was achieved at a max load of 80 N. Berselli et al. [7] used a singular, circular DEA that was deforming out of plane to generate linear motion. A compliant frame was utilized to create either unidirectional or bidirectional devices that could reset themselves to the starting position. The design of the compliant frame and the elastomer was optimized to achieve the desired actuation force. Cao and Conn [1] optimized the stoke and work output of a circular DEA that was deformed out of plane through multiple means: spring, biasing mass, and rigid support in a double cone configuration. It was discovered that as a general rule of thumb the higher stroke values were achieved for lower a/b ratios (see Fig. 1c), and higher work output was attained somewhat larger a/b ratios. The biasing mass provided the highest work output, and the double cone with the rigid support had the largest stroke.

Recognizing its various commercial applications, He et al. [8] pioneered a derivation for the equations of state for a DEA circular membrane undergoing axisymmetric OPD. The obtained system of differential algebraic equations were based on the neo-Hookean hyperelastic model and constant-permittivity assumptions. Here, those results are expanded into a numerical solution structure that contains details for its practical use. The resulting work provides an easy-to-follow framework for implementation that can be useful to both researchers and developers. Examples of how this solution framework can be implemented are presented using practical values of the parameters involved.

2 System Modeling

2.1 Out-of-Plane Deformation

When a circular membrane is deformed out of plane, it forms a conical shape. If this deformation is through the center, then the resulting cone is axisymmetric and is referred to as a *single conical dielectric elastomer actuator* (SCDEA) [1] as is shown in Fig. 1. To avoid very large stresses, a distributed loading is applied over some finite area in the neighbourhood of the membrane's center [12]. In practice, a SCDEA is created as follows. A circular disk is cut out of an elastomeric membrane of thickness T. This membrane is then prestretched over a rigid ring of radius b after which it is coated on both sides with a compliant electrode. Subsequently, the membrane is deformed out of plane by means of a force F applied to the rigid disk of radius a. There are multiple ways of applying this force seen in Fig.1c [1, 13]. In this case, the force is assumed to be constant, yet the means of applying it is not specified. The origin of the system, O, is taken at the intersection of the axis of symmetry and the top face of the rigid ring, $\mathcal{S}$. Points A and B on the membrane are located at the boundaries of the rigid disk and rigid ring, respectively, as seen in a cross-sectional view (see Fig. 1c). An arbitrary point of interest is denoted as R. Point R starts on the undeformed membrane and moves to a new position on the deformed membrane that is denoted by the coordinates $r(R)$ and $z(R)$.

In order to properly examine the kinematics of point R, the stretches present in the membrane must first be defined. This elastomer is modeled using three principal stretches that characterize the membrane in the deformed state: λ_1, λ_2, and λ_3. The longitudinal stretch, λ_1, describes the deformation in the direction from the rigid ring to the center disc. The latitudinal or circumferential stretch, λ_2, points in the circumferential direction around the cone and at a right angle to λ_1. Lastly, λ_3 is in the thickness direction. The stretches are illustrated in Fig. 1f.

[1] Obviously, this is true for any deformable membrane but our focus is on DE membranes. In addition, an extension of SCDEA, the double conical dielectric elastomer actuator (DCDEA) involves other complexities not considered here. For DCDEA applications see [9],[10], and [11].

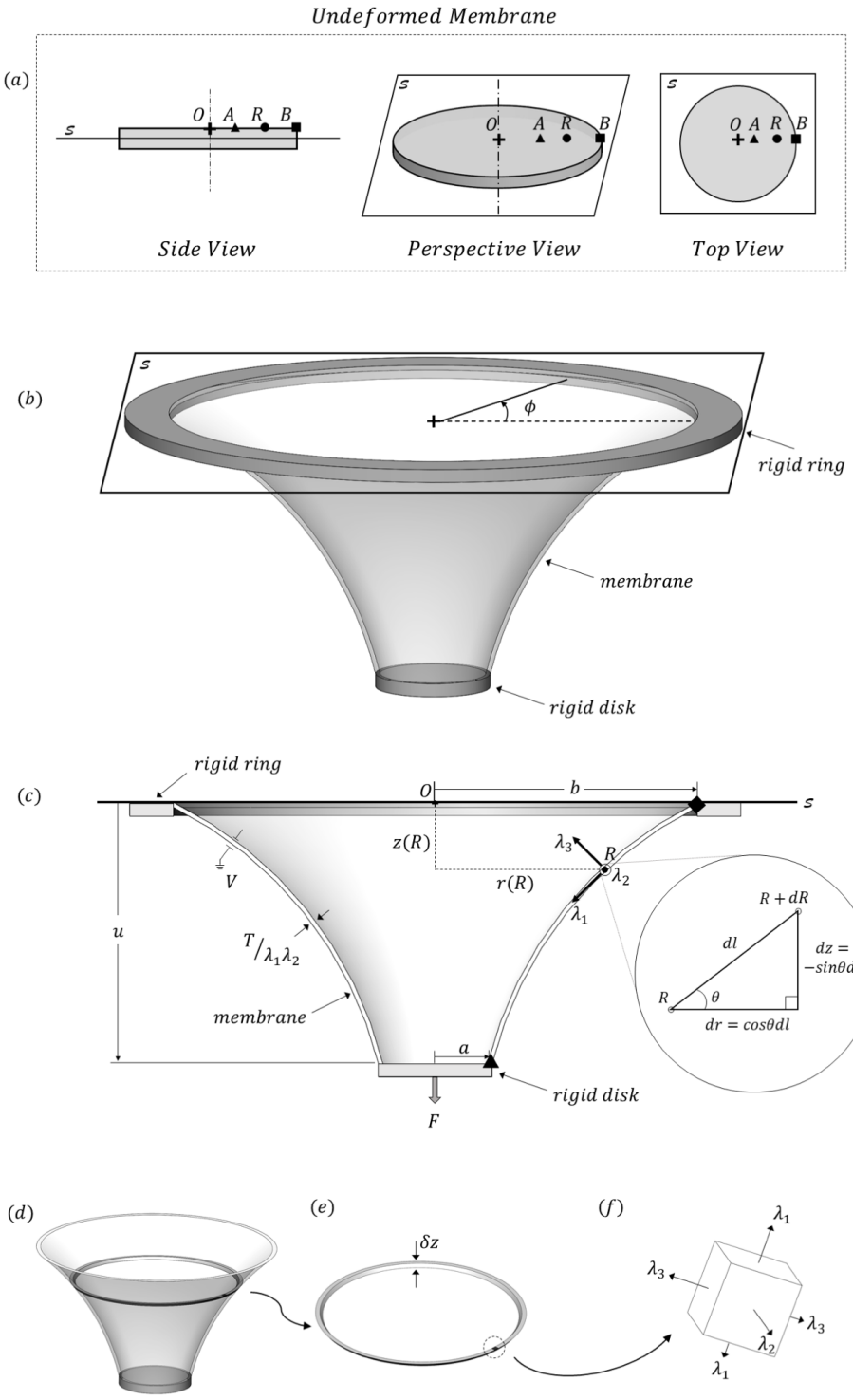

Figure 1: Diagram of a SCDEA. (a): side, perspective, and top views of unstretched and undeformed dielectric elastomer membrane. (b): Perspective view of pre-stretched and deformed DE membrane due to the action of a distributed loading acting downward (not shown in the figure) via a rigid center disk, forming a conical shape. (c) cross-section of stretched and deformed DE membrane showing a concentrated force F, and direction of stretches. (d): SCDEA showing a parcel ring with infinitesimal thickness,δz, which is emphasized in (e). (f): Stretch state of small parcel in the ring material showing main stretches, λ_1, λ_2, and λ_3. Compare the latter with those shown at point (r(R),z(R)) in sub figure(c).

Consider a point R on the undeformed membrane and a point $R+dR$ that is infinitesimally adjacent to it. As the membrane is stretched and deformed out of plane the two points move away from each other so that in the final state they are separated by a distance dl. Assuming this infinitesimal distance is a straight line yields the right triangle shown in the cutout in Fig. 1c, where θ is defined as the angle between horizontal axis and the tangent to the curve at point R in the deformed state. This causes the two legs of the triangle to be $dz = -\sin\theta dl$ and $dr = \cos\theta dl$. By using the Pythagorean theorem, dl can be written in terms of dr and dz: $dl = \sqrt{(dr)^2 + (dz)^2}$. Dividing through by dR (the distance between the points R and $R + dR$ in the undeformed state) provides the longitudinal stretch λ_1:

$$\lambda_1 = \sqrt{\left(\frac{dr}{dR}\right)^2 + \left(\frac{dz}{dR}\right)^2}. \tag{1}$$

The latitudinal stretch, λ_2, is defined as the ratio of the circumference at the point R in the deformed state versus the undeformed state due to rotational symmetry of the cone about the z-axis. This results in λ_2 being defined as $2\pi r(R)/2\pi R$. By canceling the 2π out of the numerator and denominator, we arrive at

$$\lambda_2 = \frac{r}{R}. \tag{2}$$

The third stretch, λ_3, is a ratio of the thickness of the elastomer in the deformed state versus the undeformed state. Using the assumption of incompressibility, the following equation holds true: $1 = \lambda_1\lambda_2\lambda_3$. Therefore, λ_3 can be written in terms of λ_1 and λ_2 as

$$\lambda_3 = \frac{1}{\lambda_1\lambda_2}. \tag{3}$$

The compliant electrodes on each side of the elastomer act like soft plates in a compliant parallel-plate capacitor, and the membrane is the medium. As a voltage, V, is applied across these electrodes, a charge accumulates. Here, Q is the total electric charge on the conical elastomer. As the charge builds up, the two opposite electrodes attract each other. However, since the material is considered incompressible, λ_1 and λ_2 increase as λ_3 decreases, resulting in the motion of the DEA.

The charge on the electrodes is found using the nominal electric displacement $\tilde{D}$ which is the charge on a deformed element divided by the area of an undeformed element. This definition lends itself to easy calculation of the total charge since all calculations can be done with respect to the undeformed elastomer which has much simpler geometry. By multiplying $\tilde{D}$ by the undeformed area of an element, the true charge of the deformed element can be calculated. However, since the value of $\tilde{D}$ varies at each R position, the total charge on the deformed elastomer has to be calculated by integrating across the surface of the undeformed elastomer using infinitesimal rings of width dR. The lower and upper bounds of the integral would be A and B respectively since that is the area that is covered with electrode.

$$Q = 2\pi \int_A^B \tilde{D} R dR \tag{4}$$

This system is then analyzed using the Helmholtz free energy, $\mathcal{H}$, under the assumption that the DEA is an isothermal and isochoric system [14]. By letting W be the Helmholtz free energy density of an element in the deformed state with respect to the volume of the undeformed elastomer, one can calculate the total Helmholtz free energy of the system:

$$\mathcal{H} = T \int\int W R dR d\phi \tag{5}$$

where ϕ is the azimuthal angle that sweeps around the z-axis. In our case this equation could be simplified to a single integral since there is symmetry about the z-axis.

Using the Helmholtz free energy approach, the energy can be analyzed via two pairs of work-conjugates: the force and displacement and the voltage and charge. This approach combines the work done through mechanical and electrical means to achieve equilibrium. A small change in the Helmholtz free energy can be represented by a small variations of the vertical position or charge:

$$\delta\mathcal{H} = F\delta u + V\delta Q. \tag{6}$$

By examining a small delta in W, we get the following equation due to the mechanical work done in the λ_1 and λ_2 directions and the electrical work:

$$\delta W = s_1 \delta\lambda_1 + s_2 \delta\lambda_2 + \tilde{E}\delta\tilde{D} \tag{7}$$

where s_1 and s_2 are the nominal stresses in the λ_1 and λ_2 directions, respectively. Also, $\tilde{E}$ is the nominal electric field defined as V/T. Suo's work on dielectric elastomers [14] provides a detailed derivation of these fundamental equations.

In order to further understand Eq. (7), consider a small variation in λ_1 that is caused by small changes in r and z. The small change in λ_1 can be obtained by manipulating Eq. (1). Using the cutaway in Fig. 1c and the Pythagorean theorem, the equation $dl^2 = dr^2 + dz^2$ follows naturally. By writing one of the dr terms and one of the dz terms in terms of θ and dl, $dl^2 = dl\cos\theta dr - dl\sin\theta dz$. Dividing through by dl reduces the equation to $dl = \cos\theta dr - \sin\theta dz$. Dividing through by dR results in an alternative equation for λ_1: $\lambda_1 = \cos\theta\frac{dr}{dR} - \sin\theta\frac{dz}{dR}$. A small variation in λ_1 is achieved by varying r and z by small amounts. This results in λ_1 becoming $\delta\lambda_1$, r becoming δr, and z becoming δz which leads to Eq. (8):

$$\delta\lambda_1 = \cos\theta\frac{d(\delta r)}{dR} - \sin\theta\frac{d(\delta z)}{dR}. \tag{8}$$

By the same reasoning, Eq. (2) can be re-written as

$$\delta\lambda_2 = \frac{\delta r}{R}. \tag{9}$$

Substituting Eq. (7) into Eq. 5 and setting the result equal to Eq. (6) leads to

$$2\pi T\int_A^B \delta W R dR = F\delta u + V\delta Q. \tag{10}$$

By substituting Eqs. (8) and (9) into Eq. (7) and the result into Eq. (10), the following expression emerges for the left hand side of the aforementioned equation:

$$2\pi T\int_A^B \left[s_1\left(\cos\theta\frac{d(\delta r)}{dR} - \sin\theta\frac{d(\delta z)}{dR}\right) + s_2\frac{\delta r}{R} + \tilde{E}\delta\tilde{D}\right] R dR. \tag{11}$$

Splitting the integral into individual terms leads to

$$2\pi T\left[\int_A^B Rs_1\cos\theta\frac{d(\delta r)}{dR}dR - \int_A^B Rs_1\sin\theta\frac{d(\delta z)}{dR}dR + \int_A^B s_2\delta r dR + \int_A^B R\tilde{E}\delta\tilde{D}dR\right]. \tag{12}$$

The last two terms of this expression are already completely reduced. However, the first two terms can be further simplified. Integration by parts will be used for this ($\int udv = uv - \int vdu$). For the first term, choose $u = Rs_1\cos\theta$ and $dv = \frac{d(\delta r)}{dR}dR$. Integrating by parts results in $(Rs_1\cos\theta\delta r)|_A^B - \int_A^B \delta r\frac{d(Rs_1\cos\theta}{dR}dR$. The second term in solved in a similar manner with $u = Rs_1\sin\theta$ and $dv = \frac{d(\delta z)}{dR}dR$ resulting in $(-Rs_1\sin\theta\delta z)|_A^B + \int_A^B \delta z\frac{d(Rs_1\sin\theta)}{dR}dR$. Grouping like terms together from these and the other two terms in Eq. (12) results in Eq. (13).

$$\begin{aligned} 2\pi T\int_A^B \delta W R dR = 2\pi T\Bigg[&(Rs_1\cos\theta\delta r - Rs_1\sin\theta\delta z)\Big|_A^B + \int_A^B \Bigg\{\left[-\frac{d(Rs_1\cos\theta)}{dR} + s_2\right]\delta r \\ &+ \frac{d(Rs_1\sin\theta)}{dR}\delta z + R\tilde{E}\delta\tilde{D}\Bigg\}dR\Bigg] \end{aligned} \tag{13}$$

Since $\delta r(R)$, $\delta z(R)$, and $\delta\tilde{D}(R)$ vary independently of each other, their respective terms can be isolated and examined independently of the others. This is accomplished by setting the two variables that are not being considered to zero.

Set $\delta r(R) = 0$ and $\delta\tilde{D}(R) = 0$ to look at the $\delta z(R)$ terms while using Eq. (12) as the left hand side for Eq. (10).

$$2\pi T\left[\int_A^B Rs_1\cos\theta\cancelto{0}{\frac{d(\delta r)}{dR}}dR - \int_A^B Rs_1\sin\theta\frac{d(\delta z)}{dR}dR + \int_A^B s_2\cancelto{0}{\delta r}dR + \int_A^B R\tilde{E}\cancelto{0}{\delta\tilde{D}}dR\right] = F\delta u + \cancelto{0}{V\delta Q} \quad (14)$$

$$-\int_A^B Rs_1\sin\theta\frac{d(\delta z)}{dR}dR = \frac{F}{2\pi T}\delta u \quad (15)$$

Eliminating dR from the left hand size of Eq. (15) and noticing that the linear distributed loading $2\pi s_1 R\sin(\theta)$ is constant[2] throughout the membrane (i.e., from A to B), then, in particular, it must independent of δz. Therefore, one can rewrite Eq. (15) as:

$$-Rs_1\sin\theta\int_A^B d(\delta z) = \frac{F}{2\pi T}\delta u. \quad (16)$$

The small vertical displacement δu of the center disk must be equal to the total contribution of each small δz at every parcel of the material (see Fig. 1), that is:

$$-\int_A^B d(\delta z) = \delta u \quad (17)$$

where the negative sign is due to the convention originally established (see Fig. 1). Therefore:

$$F = 2\pi T R s_1\sin\theta. \quad (18)$$

In order to look at $\delta r(R)$ terms independently, set $\delta z(R) = 0$ and $\delta\tilde{D}(R) = 0$.

$$2\pi T\left[(Rs_1\cos\theta\delta r - Rs_1\sin\theta\cancelto{0}{\delta z})\Big|_A^B + \int_A^B\left\{\left[-\frac{d(Rs_1\cos\theta)}{dR} + s_2\right]\delta r \quad + \frac{d(Rs_1\sin\theta)}{dR}\cancelto{0}{\delta z} + R\tilde{E}\cancelto{0}{\delta\tilde{D}}\right\}dR\right]$$
$$= F\delta u + \cancelto{0}{V\delta Q} \quad (19)$$

$$Rs_1\cos\theta\delta r\Big|_A^B + \int_A^B\left[-\frac{d(Rs_1\cos\theta)}{dR} + s_2\right]\delta r dR = \frac{F\delta u}{2\pi T} \quad (20)$$

Let's consider Eq. (20) briefly. The term on the right hand side of Eq. (20) must vanish since all small contributions of δz have been set to zero; therefore, there is no external work in the vertical direction. Now, let's examine the first term in Eq. (20). For every initial particle of material R, the component principal internal force $2\pi RTs_1\cos\theta$ acts perpendicular to the direction of the external force F in Fig. 1. Therefore the small internal work produced by such a horizontal force due to small horizontal displacement δr is given by $2\pi RTs_1\cos\theta\delta r$. By problem definition, the work done at the fixed boundary particles A or B must vanish and thus their difference $2\pi RTs_1\cos\theta\delta r\Big|_A^B$. Therefore:

$$2\pi RTs_1\cos\theta\delta r\Big|_A^B = 0 \quad (21)$$

or, since $2\pi T$ is non zero,

$$Rs_1\cos\theta\delta r\Big|_A^B = 0 \quad (22)$$

[2]This is based on the assumptions that the material is homogeneous and that after a force F is applied, equilibrium is allowed to be reached.

which corresponds to the first term in Eq. (20). In turn, it can be rewritten as:

$$\int_A^B \frac{d(Rs_1\cos\theta)}{dR}dR = \int_A^B s_2 dR \tag{23}$$

which leads to a function for the nominal stress in the λ_2-direction as:

$$s_2 = \frac{d(Rs_1\cos\theta)}{dR}. \tag{24}$$

Finally, by setting the two mechanical variables to zero, $\delta r(R) = 0$ and $\delta z(R) = 0$, the electrical equation can be acquired. For this case the equation reduces to

$$\begin{aligned} 2\pi T\Bigg[(Rs_1\cos\theta\cancelto{0}{\delta r} - Rs_1\sin\theta\cancelto{0}{\delta z})\Big|_A^B + \int_A^B \Bigg\{\left[-\frac{d(Rs_1\cos\theta)}{dR} + s_2\right]\cancelto{0}{\delta r} \\ + \frac{d(Rs_1\sin\theta)}{dR}\cancelto{0}{\delta z} + R\tilde{E}\delta\tilde{D}\Bigg\}dR\Bigg] = F\cancelto{0}{\delta u} + V\delta Q. \end{aligned} \tag{25}$$

We can turn the charge equation (Eq. (4)) into a small charge by changing $\tilde{D}$ to a small change, $\delta\tilde{D}$. The area for the integration remains the same.

$$\delta Q = 2\pi\int_A^B \delta\tilde{D}RdR \tag{26}$$

Substituting Eq. (26) into Eq. (25), we get:

$$\cancel{2\pi}T\int_A^B R\tilde{E}\delta\tilde{D}dR = V\cancel{2\pi}\int_A^B \delta\tilde{D}RdR. \tag{27}$$

However, the nominal electric field, $\tilde{E}$, is not dependent on R since it is by definition only dependent on the voltage (which is invariant to deformation) and the original thickness, T. This allows $\tilde{E}$ to be pulled out of the integral.

$$T\tilde{E}\cancel{\int_A^B \delta\tilde{D}RdR} = V\cancel{\int_A^B \delta\tilde{D}RdR} \tag{28}$$

This verifies the equation for the nominal electric field.

$$V = T\tilde{E} \tag{29}$$

2.2 Material Model

A hyperelastic material model is used to describe the mechanical behavior of the elastomer, providing the equations for s_1 and s_2. Numerous of these models are used for DEAs, and descriptions of some of the most common models are described elsewhere [**?**, 15, 16, 17]. Generally, these models are based on strain energy density. However, since the DEA is not solely mechanical, but also receives electrical inputs, the material model must be combined with a model for the dielectric energy density to create a combined energy density function, W. The material model will be denoted a W_M. The dielectric energy density is W_{DE}. Combining these two results in

$$W = W_M + W_{DE}. \tag{30}$$

In order to simplify the calculations, certain assumptions are made that result in an ideal dielectric elastomer. According to [14], the assumptions for ideal dielectric elastomer are as follows: (1) constant

permittivity [3] ($E = D/\varepsilon$) and (2) incompressibility ($\lambda_1\lambda_2\lambda_3 = 1$). This allows the dielectric energy density to be expressed as

$$W_{DE} = \frac{1}{2}\varepsilon E^2 = \frac{\tilde{D}^2}{2\varepsilon}\lambda_1^{-2}\lambda_2^{-2} \tag{31}$$

using the relationship $E = D/\varepsilon = \tilde{D}/(\varepsilon\lambda_1\lambda_2)$ where E is the true electric field, D is the true electric displacement, and ε is the absolute permittivity of the material.

In calculating the material behavior, the internal stress state and electric displacement are required. The in-plane nominal stresses, s_1 and s_2, and nominal electric field, $\tilde{E}$, are:

$$s_1 = \frac{\partial W}{\partial \lambda_1} \tag{32}$$

$$s_2 = \frac{\partial W}{\partial \lambda_2} \tag{33}$$

$$\tilde{E} = \frac{\partial W}{\partial \tilde{D}} \tag{34}$$

Much more detail about the derivation of these equations can be found in [14].

For the sake of simplicity, the neo-Hookean model is chosen to describe the behavior for the SCDEA. The neo-Hookean material model falls under the physically motivated models [20]. The neo-Hookean describes the behavior of hyperelastic materials for small to moderate strains because the stretch is not limited by the extension of the molecular chains. This model could prove useful in applications that use small prestretches and small actuation values. However, it was ultimately chosen for its mathematical simplicity. The material model part of Eq. (30) is displayed below:

$$W_M(\lambda_1, \lambda_2, \lambda_3) = \frac{\mu}{2}(\lambda_1^2 + \lambda_2^2 + \lambda_3^2 - 3). \tag{35}$$

Here μ is the small strain shear modulus. Combing this with the dielectric energy density presented above results in

$$W(\lambda_1, \lambda_2, \tilde{D}) = \frac{\mu}{2}(\lambda_1^2 + \lambda_2^2 + \lambda_1^{-2}\lambda_2^{-2} - 3) + \frac{\tilde{D}^2}{2\varepsilon}\lambda_1^{-2}\lambda_2^{-2}. \tag{36}$$

Using Eqs.(32)-(34) the following three equations can be calculated:

$$s_1 = \frac{\partial W}{\partial \lambda_1} = \mu(\lambda_1 - \lambda_1^{-3}\lambda_2^{-2}) - \frac{\tilde{D}^2}{\varepsilon}\lambda_1^{-3}\lambda_2^{-2} \tag{37}$$

$$s_2 = \frac{\partial W}{\partial \lambda_2} = \mu(\lambda_2 - \lambda_2^{-3}\lambda_1^{-2}) - \frac{\tilde{D}^2}{\varepsilon}\lambda_2^{-3}\lambda_1^{-2} \tag{38}$$

$$\tilde{E} = \frac{\partial W}{\partial \tilde{D}} = \frac{\tilde{D}}{\varepsilon}\lambda_1^{-2}\lambda_2^{-2}. \tag{39}$$

3 Numerical Solution

3.1 System of Equations

The following system of four equations completely describes the motion of the system due to electrical and mechanical inputs.

$$\frac{dr}{dR} = \lambda_1 \cos\theta \tag{40}$$

$$\frac{dz}{dR} = -\lambda_1 \sin\theta \tag{41}$$

[3] It is known, however, that permittivity is dependent on stretch [18, 19], and more accurate models should reflect that (work in progress).

$$\frac{d\theta}{dR} = -\frac{s_2}{s_1 R}\sin\theta \tag{42}$$

$$0 = 2\pi T R s_1 \sin\theta - F \tag{43}$$

Equations (40) and (41) naturally precipitate from Eq. (1). Equation (42) comes from a combination of Eqs. (18) and (24). Equation (43) is just Eq. (18) rewritten. Besides the aforementioned, several other relationships in this article were used to simplify the system (40)-(43) into terms of only four variables, namely r, θ, z, and λ_1.

The system is subjected to the following boundary conditions (BCs):

$$r(A) = a,\ r(B) = b,\ z(B) = 0. \tag{44}$$

These are all the result of geometric constraints. The first two BCs at r are defined by the radius of the inner and outer rigid supports, respectively. The condition at z is due to the definition of the r-z coordinate system. Furthermore, the following dimensionless forms from He et al. [8] were used to non-dimensionalize the system of equations for easier comparison: u/a, $Q/(2\pi a^2\sqrt{\varepsilon\mu})$, $F_n = F/(2\pi a T\mu)$, and $V_n = V/(T\sqrt{\mu/\varepsilon})$.

The resulting system of equations is what is known as a differential-algebraic equation (DAE) system. As the name implies these DAE systems contain both differential and algebraic equations, where the algebraic equations are often constraint equations. We will focus on semi-explicit DAE systems such as ours that take the form [21]:

$$\frac{d\mathbf{x}}{dt} = \mathbf{f}(\mathbf{x}, \mathbf{y}, t) \tag{45}$$

$$0 = \mathbf{g}(\mathbf{x}, \mathbf{y}, t) \tag{46}$$

Here the $\mathbf{x}$ variables are those that occur both in derivative form and algebraic form. Whereas the $\mathbf{y}$ variables only occur in the algebraic form even though they may appear in both the $\mathbf{f}$ and $\mathbf{g}$ function, and t is the independent variable. This is what separates an ODE system from a DAE system.

3.2 Implementation of Numerical Method

A boundary value problem (BVP) DAE system of this type must be solved numerically. Here, a more comprehensive (as compared to [8] & [1]) numerical algorithm is provided for solving the system of equations, Eqs. (40) - (44), with the goal of providing a framework for easy implementation. Information on how to solve BVP DAE systems is scarce to find. In some of the most common commercially available packages, direct solvers that can directly handle these BVP DAE systems were not found. Therefore, a combination of functions were consolidated into a customized routine. One way of solving a BVP is to transform it into an initial value problem (IVP). This is accomplished through the shooting method, which is summarized as follows (see Fig. 2). An initial value is guessed; the solution is calculated and the result is compared to the known BC; then an adjustment is made to the initial guess; this updated guess is used to repeat the process until the solution converges. An existing ODE solver was used inside of our implementation of the shooting method algorithm, which is shown in Fig. 2. The algebraic equation was used to generate consistent initial conditions.

The developed algorithm follows the logic of the flow chart in Fig. 2. MATLAB® was chosen to solve this system of equations due to its perceived familiarity and availability. The algorithm begins with the definition of the global parameters and an initial guess for λ_1. The input parameters defined were F_n, V_n, a/A, and b/B. The λ_1 guess is based on the prestretch for the particular application. Next, Eq. (43) is used to calculate a value for θ based on initial conditions, r, R, and the guessed λ_1. The algebraic constraint Eq. (43) is used for this in a dimensionless form. However, the λ_1 value is kept as a variable, and only the r and R values are defined using the BCs at B. Now that a set of consistent initial conditions is defined, the system of equations, Eqs. (40) - (43) can be written in matrix form according to Eq. (47) and Eq. (48), where M is the mass matrix:

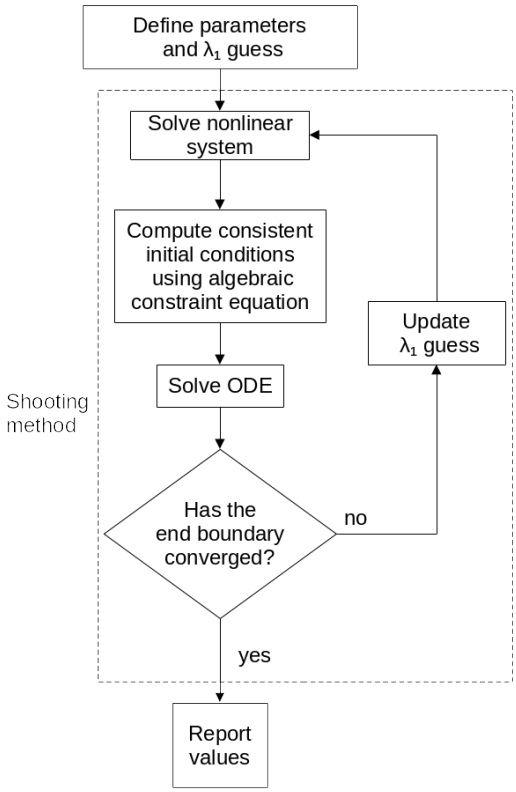

Figure 2: Flowchart of algorithm for solving the DAE system based on a shooting method. Note that an extra step is needed in order to ensure that consistent initial conditions are computed based on the nondimensionlized algebraic algebraic obtained from Eq. (18).

$$\mathbf{M}\frac{d\boldsymbol{\chi}}{dR} = \mathbf{f}(\boldsymbol{\chi}, R). \tag{47}$$

Where

$$\mathbf{M} = \begin{bmatrix} 1 & 0 & 0 & 0 \\ 0 & 1 & 0 & 0 \\ 0 & 0 & 1 & 0 \\ 0 & 0 & 0 & 0 \end{bmatrix}, \boldsymbol{\chi} = \begin{bmatrix} r \\ z \\ \theta \\ \lambda_1 \end{bmatrix}, \text{ and } \frac{d\boldsymbol{\chi}}{dR} = \begin{bmatrix} dr \\ dz \\ d\theta \\ d\lambda_1 \end{bmatrix}. \tag{48}$$

This system is then solved over the span $[B, A]$ using the two conditions at B defined above, the calculated θ value, and the variable for the unknown λ_1. The first order DAE system is then solved using the ode15s function in MATLAB®. Then, the remaining BC is applied ($r(A) = a$). This means that the calculated value of $r(A) - a$ should equal zero if the BC is satisfied. The fsolve function is used to drive this quantity to zero by adjusting the value of λ_1. This iteration is the shooting method portion of the code. Once convergence is achieved, the λ_1 guess is updated with the current λ_1 value. This will be used as the next guess for the next voltage term. This becomes important as the voltage terms become larger and the difference between λ_1 values becomes larger. Increasingly smaller steps might need to be taken to facilitate convergence. Once this occurs, the program ends the loop and reports the following results: R, r, z, θ, λ_1, and λ_2. These values are then used to make a variety of plots.

4 Results and Discussion

4.1 General Behavior

In order to gain more understanding into the parameter-dependent behavior of the SCDEA, the force, voltage, and geometry were varied. In addition, a few example cases are evaluated using a typical range of reported values in the literature. Therefore, our results can be applicable for future studies. Figure 3 is a cutout from Fig. 1 and is included here for convenience as a reference for the stretches. Unless otherwise specified, the following parameters were used throughout this section: a rigid disk radius of $a = 0.008m$, a rigid ring radius of $b = 4a$, and ratios relating the prestretch $A = a/1.2$ and $B = b/1.2$.

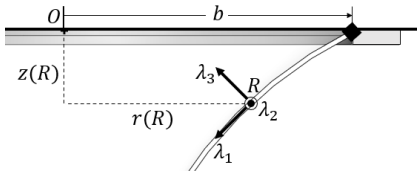

Figure 3: Clarifying cutout for stretches

The first scenario explored was that of a constant voltage with varying applied forces. Figures 4 - 7 show how F_n ranging from 1 to 3.5 affects the shape of the cone as well as the stretches within the cone at certain fixed voltages. For ease of comparison, the range of the vertical axes has been maintained across this set of figures.

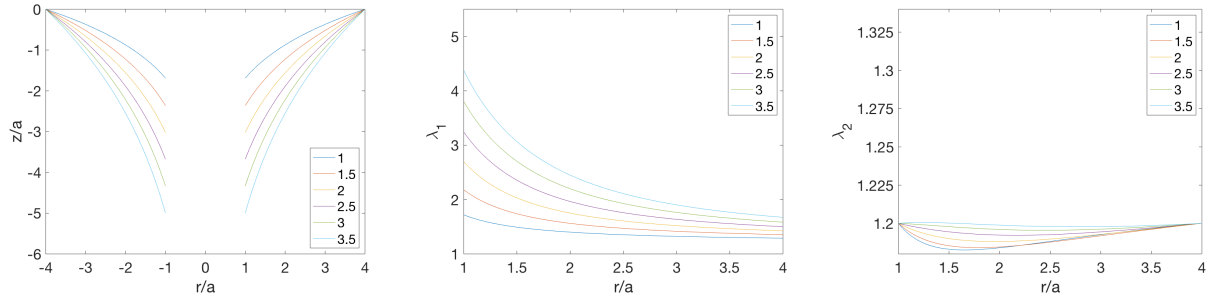

(a) deformation (b) longitudinal stretch (c) circumferential stretch

Figure 4: Dimensionless deformation and stretch graphs for various applied dimensionless forces at $V_n = 0$.

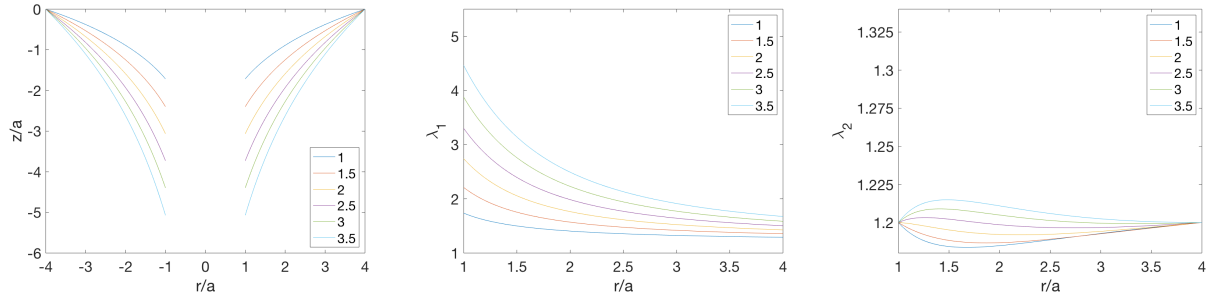

(a) deformation (b) longitudinal stretch (c) circumferential stretch

Figure 5: Dimensionless deformation and stretch graphs for various applied dimensionless forces at $V_n = 0.1$.

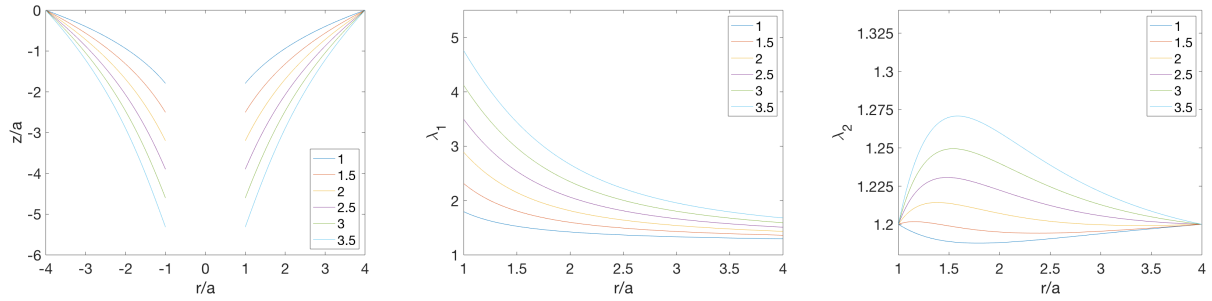

(a) deformation (b) longitudinal stretch (c) circumferential stretch

Figure 6: Dimensionless deformation and stretch graphs for various applied dimensionless forces at $V_n = 0.2$.

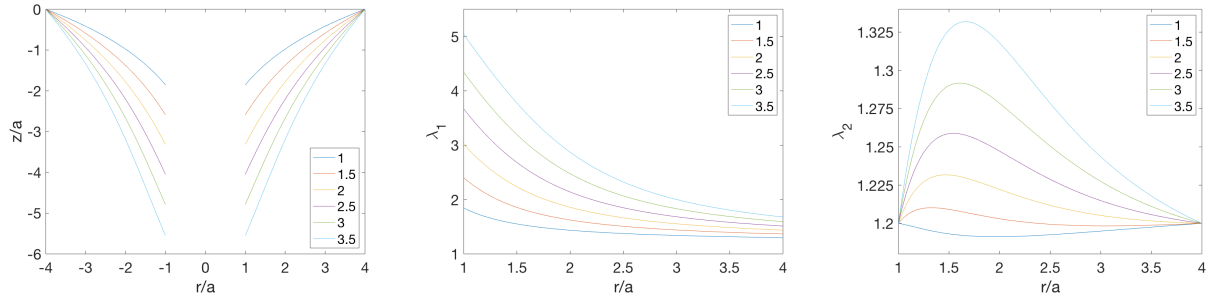

(a) deformation (b) longitudinal stretch (c) circumferential stretch

Figure 7: Dimensionless deformation and stretch graphs for various applied dimensionless forces at $V_n = 0.25$.

For the purely mechanical case, the voltage is zero (see Fig. 4). Here the general behavior can be observed. As would be expected and can be seen in Fig. 4a, the cone elongates in the z-direction under increasing load from approximately -1.6 to -5. Figure 4b shows how the longitudinal stretch increases as more force is applied. Note that there is a much more drastic change in longitudinal stretch closer to the rigid disk. This is due to the fact that the tangent angle farther down the cone (closer to the tip) is larger; therefore, the force is directed more parallel to the λ_1-direction near the tip of the cone while less near the base. Figure 4c shows the circumferential stretch (λ_2) in the cone. This stretch is restricting the cone from expanding in diameter. While its range is smaller than that of λ_1, λ_2 approaches the initial prestretch as the force exerted on the cone is increased. It is interesting to note that λ_2 at small forces is actually less than the initial prestretch. That means that there is a small degree of relaxation in the circumferential direction at low applied forces. However, the stretch remains above unity, indicating that there is still some restrictive force on the cone; otherwise, electromechanical instability can occur.

The overall trend for subfigures (a) is an increase in the z/a deformation, as should be expected. The zero voltage case at the highest force was around 5 whereas the maximum deformation at $V_n = 0.2$ for the highest force is around 5.6. This difference, while relatively small, is due to the actuation and thinning of the elastomer. As the elastomer is compressed in thickness the other two stretches must compensate by expanding the overall surface area. This extra area is invested towards the deformation in the height of the cone. Subfigures (b), in general, maintain a typical shape with only minor change in amplitude more on the $r/a = 1$ side (note that as force increases, these changes become more noticeable). Overall, the subfigures (c) undergo the most noticeable change. Even with slight actuation, a large spike in the circumferential stretch can be observed. This is caused when the cone is deforming in the z-direction and tries to stretch the cone into a more straight-line case where the radius, r, would increase. The circumferential stretch is the counteracting stretch in this case. However, points that were once at a tighter radius inevitably get repositioned to larger radius. A large difference can be seen here due to actuation.

The second scenario explored was that of a constant force with varying applied voltages. Figure 8 shows

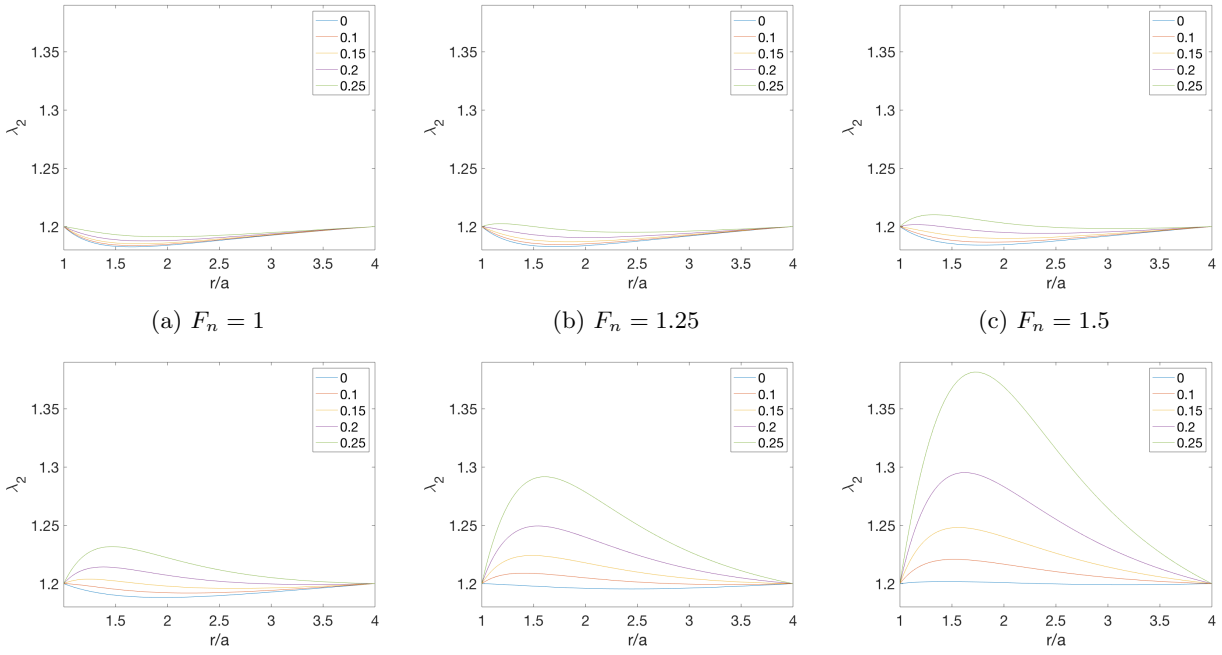

(a) $F_n = 1$ (b) $F_n = 1.25$ (c) $F_n = 1.5$

(d) $F_n = 2$ (e) $F_n = 3$ (f) $F_n = 4$

Figure 8: Circumferential stretch graphs for various applied dimensionless voltages at various fixed forces.

how voltages ranging from 0 dimensionless units to 0.25 affect the circumferential stretch within the cone at different discrete dimensionless force values ranging between 1 and 4. Again, the vertical axis range was maintained throughout the figure. Only the λ_2 stretch is considered here because the deformation and λ_1 graphs did not add any significant new information. As can be seen in Figs. 4 - 7, the greater the force, the greater the elongation would be. As voltage is applied, the cone would then behave like Fig. 12a. The λ_1 stretch graphs were not included here because the behavior is the same as Fig. 12b with the λ_1 value increasing as the force increased. There was a greater increase nearer to the rigid disk than near the ring. The real graphs of interest were the λ_2 graphs. The behavior is very similar to that in the previous set of graphs in which the λ_2 value was increasing with applied voltage and force. The same behavior is observed here only displayed differently. Low force causes a low λ_2 value regardless of the applied voltage. As the force is increased, the amount of voltage inputted into the system greatly affects the amount of stretch possible in this direction, and not in a linear manner. The highest λ_2 value achieved was with the highest force ($F_n = 4$) and highest voltage ($V_n = 0.25$), resulting in a peak λ_2 value of approximately 1.38. This is an increase of 15% over the initial prestretch.

Next, the affect of changing the geometry of the cone was examined. Figures 9, 10, and 11 look at ring to disk ratios of 1.5, 4, and 6 respectively. Here only the vertical axes in subfigures (b) and (c) were kept the same as the subfigures (a) had a very large range of deformations. A dimensionless force of 2 was again used for these plots. As can be observed in Fig. 9, as the disk radius approaches that of the ring, the edges of the cone become straighter and more in-line with the applied force. This affects the longitudinal stretch, resulting in a λ_1 graph that appears a lot more linear than previous cases. As the tip of the cone becomes narrower (i.e. decrease of ratio a/b), the radius of curvature decreases which results in more extreme changes in λ_1 (see Fig. 11). As can be seen, Fig. 11b looks much more L-shaped than the nearly linear case seen in Fig. 9b even though they all have similar values near $r/a = 1$. The λ_2 graphs become less symmetrical with larger spikes both above and below the prestretch level. There is a stretch reduction for lower actuation levels and a stretch peak for higher actuations. Both the maximum and minimum values here occur well toward the rigid disk side. It is interesting to note that the overall deformation in the z-direction greatly increases as the ratio of b/a increases. A ratio of 1.5 has a deformation of z/a less than 1 while a ratio of 6 results in a deformation greater than 4. This is all with the same force. This is due to the fact that

the smaller disk is able to exert more pressure than a larger disk with the same applied force. The actual actuation then only causes small changes in the z-direction.

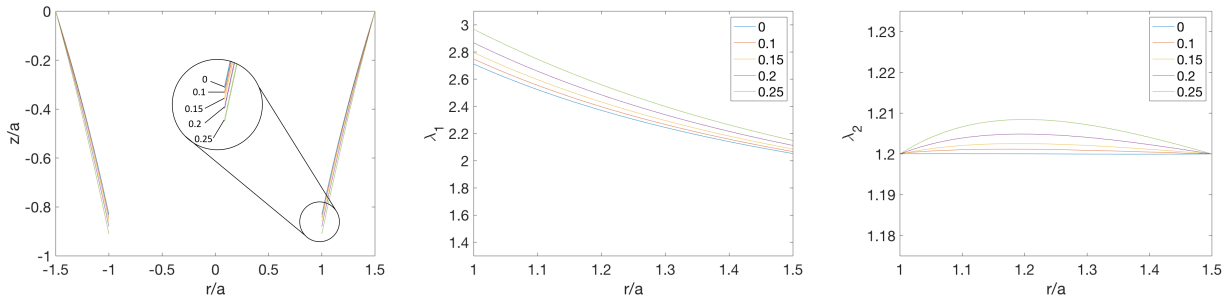

(a) deformation (b) longitudinal stretch (c) circumferential stretch

Figure 9: Dimensionless deformation and stretch graphs for ring to disk ratio of 1.5.

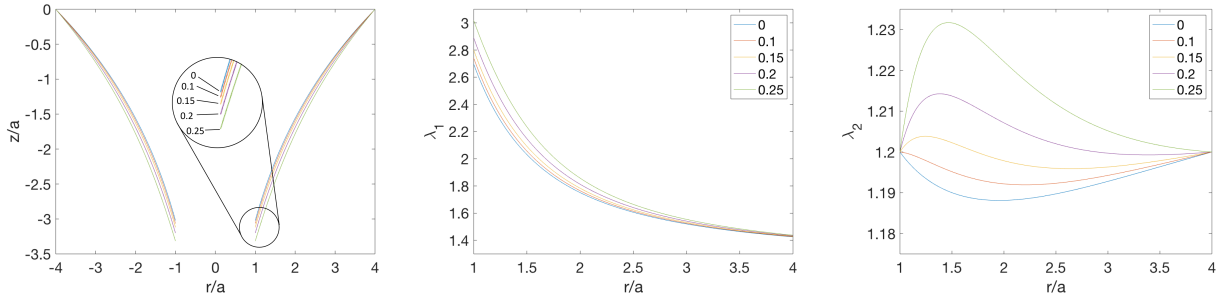

(a) deformation (b) longitudinal stretch (c) circumferential stretch

Figure 10: Dimensionless deformation and stretch graphs for ring to disk ratio of 4.

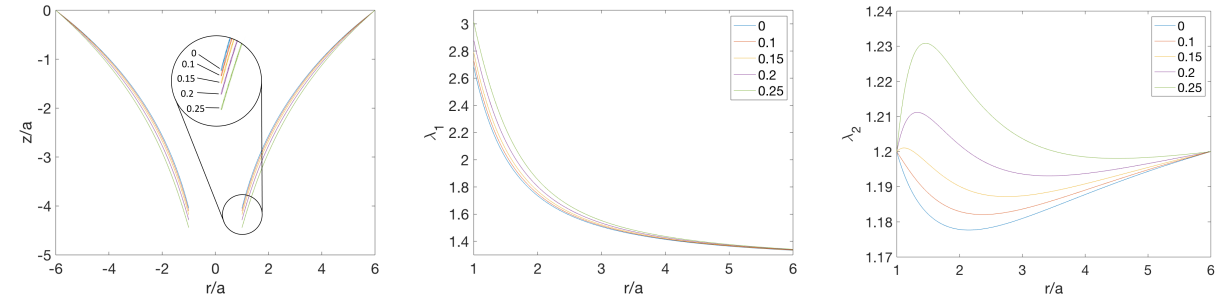

(a) deformation (b) longitudinal stretch (c) circumferential stretch

Figure 11: Dimensionless deformation and stretch graphs for ring to disk ratio of 6.

The one common attribute for all of these graphs is a prestretch of 1.2. This is on the lower side. With our experimental work, we have used a prestretch value closer to 3 for materials like VHB 4910. Therefore, adjusting this λ_p value will allow for a larger range of F_n and V_n than is presented here in this set of plots. This is just a snapshot of the general behavior of the the cone under different mechanical, electrical, and geometric conditions. An exhaustive study would not be feasible here. However, some other examples were considered that used data directly from literature that represents a wider use case.

4.2 Examples

In the sequel, three examples are presented from literature that utilize a variety of elastomeric materials, prestretches, and geometries.

4.2.1 Example 1: General Material Case

This example is based on data from He et al. [8]. The three graphs that define the deformation and two principal in-plane stretches can be seen in Fig. 12. The following parameters were used to generate the graphs: a rigid disk radius of $a = 0.008m$ (this was not given but assumed and is somewhat arbitrary as the nondimensionalized axes cancel out any dependence on a), a rigid ring radius of $b = 4a$, and ratios relating the prestretch $A = a/1.2$ and $B = b/1.2$. The nondimensionalized force F_n was set to 2 and the dimensionless voltage values were varied to be $V_n = \{0, 0.1, 0.15, 0.2, 0.25\}$. No material was listed for this theoretical study. Matching results were obtained.

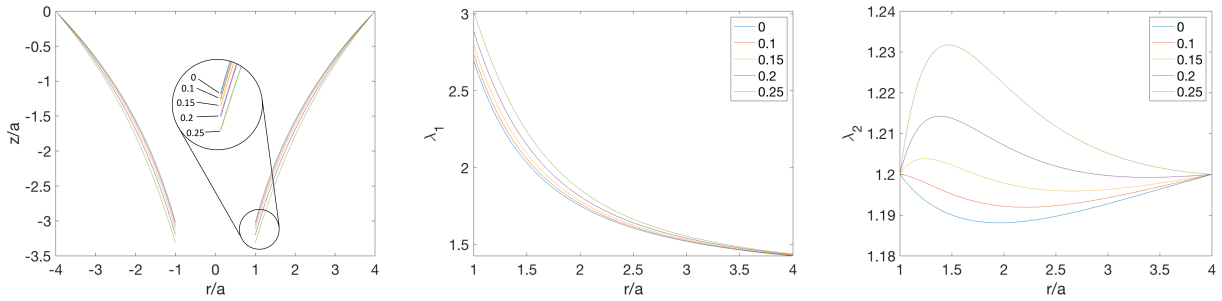

(a) deformation (b) longitudinal stretch (c) circumferential stretch

Figure 12: Example of possible state based on data from [8], using the following parameters: material not specified, $b/a = 4$, $\lambda_p = 1.2$, $F_n = 2$, $V_n = \{0, 0.1, 0.15, 0.2, 0.25\}$.

Figure 12a shows the vertical cross section of the conical DEA and how it behaves during actuation. The inner-most profile is the one where no voltage is applied. As voltage is applied the cone elongates and bows outward to become straighter. The elongation that occurs during actuation is due to the increase in λ_1 as can be seen in Fig. 12b, and the straightening of the edges is due to the increase of λ_2 at points away from the boundary. Interestingly, the peak λ_2 value shifts from the boundary at zero voltage to about $r/a = 1.5$ as the voltage is increased to $V_n = 0.25$ despite λ_1 always being strictly decreasing as one moves from the rigid disk to the outer ring ($r/a = 1 \rightarrow r/a = 4$). This aptly demonstrates the non-homogeneity of the stretches within the cone. However, at these forces and voltages, λ_1 clearly dominates as the λ_2 values vary only slightly in comparison. These graphs match the results from [8].

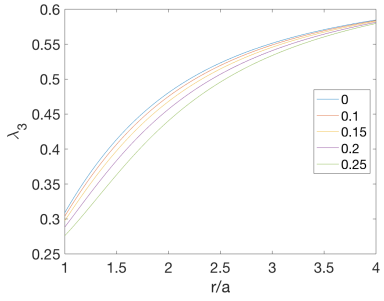

Figure 13: Thickness stretch

By combining data from Fig. 12b and c, Fig. 13 can be generated as λ_3 is just $1/\lambda_1\lambda_2$. As would be expected, the general shape of this graph is a reflection of the λ_1 graph about the horizontal axis as that behavior dominates. The thickness of the membrane is reduced by about half as one moves from the ring

to the disk. Experimental work that has been performed in our lab has shown that failure due to dielectric breakdown most often occurs right around the rigid disk ($r/a = 1$) where the thickness is at a minimum.

4.2.2 Example 2: VHB 4910 Case

The second example considered data from reported work on human pulse tracking [4]. Here, the acrylic-based elastomer VHB 4910 was used with an initial thickness $T = 1$ mm. The ring to disk radius ratio was 5.4 with $b = 68.58$ mm and $a = 12.7$ mm. A prestretch of $\lambda_p = 2$ was used in this case, which is greater than the other graphs. A dimensionless force, F_n, of 0.616 was the result of a 100 g applied mass. The voltage values covered were 1000 V, 2000 V, 2500 V, and 0 V was included for reference. This resulted in $V_n = \{0, 0.038, 0.075, 0.094\}$. The value of the small strain shear modulus for VHB 4910 was taken to be $\mu = 19.96$ kPa [22] while the dielectric permittivity $\varepsilon = 2.842 \times 10^{-11}$ F/m came from the VHB 4910 data sheet [23]. The resulting graphs can be seen in Fig. 14. For our experimental work with VHB 4910, voltages below 3000 V produce very small actuation. This is evidenced here by the lack of significant deformation. Even the λ_2 values only vary by a couple of thousandths which is almost an order of magnitude less than the other graphs previously examined. This seems to be due to a combination of the force and higher prestretch.

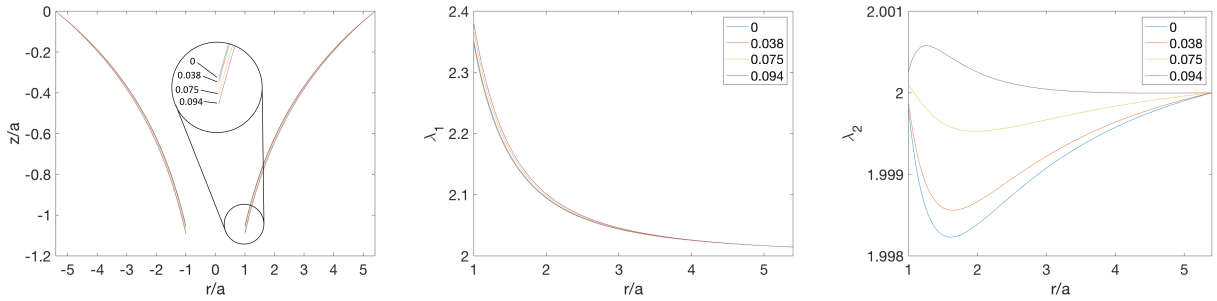

(a) deformation (b) longitudinal stretch (c) circumferential stretch

Figure 14: Example of possible state based on data from Ye et al [4]. The following parameters were used: VHB 4910, $T = 1$ mm, $b/a = 5.4$, $\lambda_p = 2$, $F_n = 0.616$, $V_n = \{0, 0.038, 0.075, 0.094\}$.

4.2.3 Example 3: Silicone Rubber Material Case

A much thinner membrane material is now examined for this third example. Parameters were used from a Cao and Conn article that investigated the work output and stroke for various geometries, prestretches, and means of out-of-plane deformation [1]. One of their cases was chosen. The material used was a 40μm silicone rubber from Parker Hannifin. The chosen geometry had $b = 20$ mm and $a = 5$ mm for a b/a ratio of 4. The prestretch was 1.2, as is typical for this type of thin silicone elastomer. A dimensionless force, F_n, of 1.91 was used. The voltage values covered were supposed to range between 0 V and 1500 V, resulting in $V_n = \{0, 0.45\}$. The value of the small strain shear modulus for this elastomer had to be calculated using the relation $2\mu = \sum_{i=1}^{N} \mu_i \alpha_i$ from [24] since the data provided was for the Ogden model. The calculated value was $\mu = 104.25$ kPa while the dielectric permittivity was $\varepsilon = 1.5 \times 10^{-11}$ F/m. The resulting graphs can be seen in Fig. 15. Here much larger deformations can be seen in subfigure (a). In addition, the variation in stretches is also much larger than observed in the other cases. Keep in mind, however, that this is all relative to the size of the cone, which in this case is very small. So, a small deformation can produce a large relative deformation when compared to overall size.

Despite having very different values for T, F_n, and V_n (as compared against the previous examples), the model is still able to predict accurately the behavior of the actuator. However, the modeling framework only seems to break down at values for which the electromechanical material model itself breaks down, as well. As it turns out, at high voltage values, the ratio of s_2 to s_1 can diverge for higher θ values (near the rigid disk) and become a double-valued function along λ1-direction. Interestingly, this is the location where electromechanical instabilities such as wrinkling has been observed, during experimental work carried out by the authors. Therefore, the full 1.5kV of voltage ($V_n = 0.45$) would not produce a converging solution.

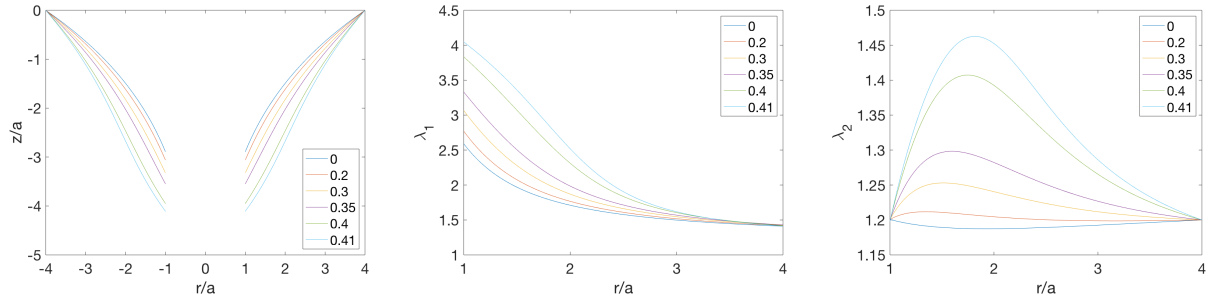

(a) deformation (b) longitudinal stretch (c) circumferential stretch

Figure 15: Example of possible state based on data from Cao and Conn [1] for a 40μm silicone rubber from Parker Hannifin. The following parameters were used: $T = 40$ μm, $b/a = 4$, $\lambda_p = 1.2$, $F_n = 1.91$, $V_n = \{0, 0.2, 0.3, 0.35, 0.4, 0.41\}$, $\mu = 104.25$ kPa, $\varepsilon = 1.5 \times 10^{-11}$ F/m.

In fact, voltages over 1.38kV ($V_n = 0.41$) resulted in difficulties when trying to find a solution that would converge. As a consequence, voltage steps (a.k.a., iteration steps) were reduced in order to find some limit where the solution still produced a reasonable result. As can be observed in Fig. 15a, a deformation graph shows signs of the elastomer bowing outwards near the rigid ring. This is a visual indication that the solution is breaking down. A proposed solution could be the inclusion of a more robust electromechanical material model.

It is worth noting that different values of terms can still result in similar behavior in the graphs. That is due to the fact that the dimensionless terms of force and voltage can mask what is going on behind the scenes. For instance, for a given dimensionless force, the radius of the disk could be doubled and the original thickness of the elastomer cut in half with no noticeable effect on F_n. Effort has been made to encompass as large of a working space as possible to make the results useful to the largest possible audience. However, it is possible that extreme cases would not be modeled without modification to the code.

5 Conclusions

The various applications of DEAs as promising transducers for robots, energy harvesting, medical devices, etc., make their study relevant and important. The axisymmetric OPD for a circular DEA membrane has been studied. Based on theoretical work previously derived, a detailed numerical solution framework has been developed and presented in this work. Implementation of the proposed framework was shown in the form of practical examples. A range of parameters were used based on reported literature and practical applications. An analytical comparison of the results was also presented.

The resulting framework has some limitations. The nature of the DAEs rendered the BVP problem solution susceptible to hyperparameters. Therefore, care must be taken when implementing the numerical solution presented. Depending on the initial guessed λ_1, integration steps, and other parameters, the $\lambda_1 - \theta$ relationship can become double-valued, which can lead to nonconverging solutions. Furthermore, since the DAEs were derived using neo-Hookean and constant-permittiviy assumptions, the resulting solution (even if based on dimensionless parameters) is limited to the aforementioned material model constraints. Future work (in progress) will expand the proposed framework to include more robust hyperelastic material models as well as stretch-dependent permittivity. In addition, future work could include more degrees of freedom for analysis.

6 Nomenclature

a = rigid disk radius
A = position of point on undeformed membrane that will end up at the edge of the rigid disk
b = rigid ring inner radius

B = position of point on undeformed membrane that will end up at the inner edge of the rigid ring
D, $\tilde{D}$ = true, nominal electric displacement
dl = the straight-line distance between R and $R + dR$ in deformed membrane
E, $\tilde{E}$ = true, nominal electric field
$\mathbf{f}$ = represents a function
F = out-of-plane applied force
F_n = nondimensionalized force
$\mathbf{g}$ = represents a function
$\mathcal{H}$ = Helmholtz free energy of the system
M = mass matrix
O = origin of cone
Q = total electric charge on membrane
r = radial position
R = point of interest on undeformed membrane
s_1 = nominal stress in λ_1-direction
s_2 = nominal stress in λ_2-direction
$\mathcal{S}$ = plane that coincides with the origin of the cone and the rigid disk
t = independent variable in a semi-explicit DAE system
T = unstretched undeformed thickness of elastomer
u = overall vertical displacement of cone
V = voltage applied across the membrane
V_n = nondimensionalized voltage
W = Helmholtz free energy density
W_{DE} = dielectric energy density
W_M = material model contribution to the free energy density
$\mathbf{x}$ = dependent variables that have a derivative present a semi-explicit DAE system
$\mathbf{y}$ = dependent variables that do not have a derivative present a semi-explicit DAE system
z = vertical position
$\delta(\cdot)$ = represents a small change in the variable, such as for r, z, $\tilde{D}$, etc.
ε = absolute permittivity of the elastomeric material
θ = angle between the horizontal axis and the tangent line at point R on the deformed membrane
λ_1 = stretch in the longitudinal direction
λ_2 = stretch in the latitudinal (circumferential) direction
λ_3 = stretch in the thickness direction
λ_p = prestretch of the membrane
μ = small strain shear modulus
ϕ = azimuthal angle (sweeps around z-axis)
$\boldsymbol{\chi}$ = matrix containing all of the dependent variables of the system

7 Conflict of Interest

The authors declare no conflict of interest relevant to this article.

References

[1] Chongjing Cao and Andrew T Conn. Performance optimization of a conical dielectric elastomer actuator. In *Actuators*, volume 7, page 32. Multidisciplinary Digital Publishing Institute, 2018.

[2] Chongjing Cao, Xing Gao, and Andrew T Conn. A magnetically coupled dielectric elastomer pump for soft robotics. *Advanced Materials Technologies*, 4(8):1900128, 2019.

[3] Philipp Linnebach, Gianluca Rizzello, and Stefan Seelecke. Design and validation of a dielectric elastomer membrane actuator driven pneumatic pump. *Smart Materials and Structures*, 2020.

[4] Zhihang Ye, Zheng Chen, Ramazan Asmatulu, and Hoyin Chan. Robust control of dielectric elastomer diaphragm actuator for human pulse signal tracking. *Smart Materials and Structures*, 26(8):085043, 2017.

[5] Steven Dubowsky, Samuel Kesner, Jean-Sébastien Plante, and Penelope Boston. Hopping mobility concept for search and rescue robots. *Industrial Robot: An International Journal*, 35(3):238–245, 2008.

[6] Eliana Bortot and Massimiliano Gei. Harvesting energy with load-driven dielectric elastomer annular membranes deforming out-of-plane. *Extreme Mechanics Letters*, 5:62–73, 2015.

[7] Giovanni Berselli, Rocco Vertechy, Gabriele Vassura, and Vincenzo Parenti-Castelli. Optimal synthesis of conically shaped dielectric elastomer linear actuators: design methodology and experimental validation. *IEEE/ASME Transactions on Mechatronics*, 16(1):67–79, 2010.

[8] Tianhu He, Xuanhe Zhao, and Zhigang Suo. Dielectric elastomer membranes undergoing inhomogeneous deformation. *Journal of Applied Physics*, 106(8):083522, 2009.

[9] Canh Toan Nguyen, Hoa Phung, Tien Dat Nguyen, Hosang Jung, and Hyouk Ryeol Choi. Multiple-degrees-of-freedom dielectric elastomer actuators for soft printable hexapod robot. *Sensors and Actuators A: Physical*, 267:505–516, 2017.

[10] Hector Medina and Carson W Farmer. Improved model for conical dielectric elastomer actuators with fewer electrical connections. *Journal of Mechanisms and Robotics*, 12(3), 2020.

[11] Chongjing Cao, Stuart Burgess, and Andrew T Conn. Toward a dielectric elastomer resonator driven flapping wing micro air vehicle. *Frontiers in Robotics and AI*, 5:137, 2019.

[12] TE Tezduyar, LT Wheeler, and L Graux. Finite deformation of a circular elastic membrane containing a concentric rigid inclusion. *International journal of non-linear mechanics*, 22(1):61–72, 1987.

[13] Philipp Loew, Gianluca Rizzello, and Stefan Seelecke. A novel biasing mechanism for circular out-of-plane dielectric actuators based on permanent magnets. *Mechatronics*, 56:48–57, 2018.

[14] Zhigang Suo. Theory of dielectric elastomers. *Acta Mechanica Solida Sinica*, 23(6):549–578bib, 2010.

[15] T Beda. An approach for hyperelastic model-building and parameters estimation a review of constitutive models. *European Polymer Journal*, 50:97–108, 2014.

[16] L Angela Mihai and Alain Goriely. How to characterize a nonlinear elastic material? a review on nonlinear constitutive parameters in isotropic finite elasticity. *Proceedings of the Royal Society A: Mathematical, Physical and Engineering Sciences*, 473(2207):20170607, 2017.

[17] Carson Farmer and Hector Medina. Dimensionless parameter-based numerical model for double conical dielectric elastomer actuators. *Engineering Research Express*, 2020.

[18] Salomón MA Jiménez and Robert M McMeeking. Deformation dependent dielectric permittivity and its effect on actuator performance and stability. *International Journal of Non-Linear Mechanics*, 57:183–191, 2013.

[19] Salomón MA Jiménez and Robert M McMeeking. A constitutive law for dielectric elastomers subject to high levels of stretch during combined electrostatic and mechanical loading: Elastomer stiffening and deformation dependent dielectric permittivity. *International Journal of Non-Linear Mechanics*, 87:125–136, 2016.

[20] Gilles Marckmann and Erwan Verron. Comparison of hyperelastic models for rubber-like materials. *Rubber chemistry and technology*, 79(5):835–858, 2006.

[21] Uri M Ascher and Linda R Petzold. *Computer methods for ordinary differential equations and differential-algebraic equations*, volume 61. Siam, 1998.

[22] Karali Patra and Raj Kumar Sahu. A visco-hyperelastic approach to modelling rate-dependent large deformation of a dielectric acrylic elastomer. *International Journal of Mechanics and Materials in Design*, 11(1):79–90, 2015.

[23] 3M Industrial Adhesives and Tapes Division. *3M VHB Tape - Specialty Tapes*, June 2020.

[24] RW Ogden, Giuseppe Saccomandi, and Ivonne Sgura. Fitting hyperelastic models to experimental data. *Computational Mechanics*, 34(6):484–502, 2004.